



First-principles design of a Dirac semimetal: An NP monolayerYaozhuang Nie ^{*}, Jianmin Zhang, Wei Chen, Qinglin Xia, Xiguang Wang, and Guang-hua Guo [†]
School of Physics and Electronics, Central South University, Changsha, 410083 China

(Received 21 February 2020; revised manuscript received 6 May 2020; accepted 15 June 2020; published 26 June 2020)

We report a two-dimensional (2D) Dirac semimetal in an orthorhombic $Pm\bar{m}a$ structure, an NP monolayer, based on first-principles calculations. The NP monolayer is found to be stable according to phonon dispersion and molecular dynamical simulations. It exhibits a pair of anisotropic Dirac cones exactly at the Fermi level, located along high symmetry lines in the Brillouin zone, and shows highly anisotropic in-plane stiffness. First-principles calculations show that Dirac cones are locally stable under strains along the x or y direction and electric fields perpendicular to the monolayer. The Dirac nodes are protected from gap opening by the mirror-reflection symmetry in the x direction. We construct an effective two-band tight-binding model to characterize the Dirac states. Our result provides a promising 2D material for special electronics applications.

DOI: [10.1103/PhysRevB.101.235443](https://doi.org/10.1103/PhysRevB.101.235443)**I. INTRODUCTION**

The discovery of graphene in 2004 has not only triggered considerable interest in exploring novel 2D materials [1–9] but also opened the world of Dirac cones and the physics that derives from them [10–15]. Since then, topological insulator, Dirac semimetals, and Weyl semimetals have attracted huge attention owing to their rich physics as well as potential applications [16–22]. These seemingly diverse materials, which we call Dirac materials, have the same Dirac fermion low-energy excitations and possess properties that are a direct consequence of the Dirac spectrum of the quasiparticles. For example, the presence of Dirac nodes in the excitation spectrum controls low-energy properties. Therefore, Dirac materials all exhibit a number of universal properties including the temperature dependence of the fermionic specific heat, response to impurities and magnetic fields, suppressed backscattering, transport properties, and optical conductivity [23].

Graphene, which is a monolayer honeycomb structure of carbon atoms, might be the most famous Dirac material [2,3,24]. In the absence of spin-orbit coupling (SOC), graphene is a 2D Dirac semimetal with its conduction band and valence band touching at the K and K' points in the Brillouin zone. The Dirac points at the K and K' points are protected by inversion symmetry, time-reversal symmetry, and C_3 symmetry [9,25,26]. The existence of Dirac points at the Fermi level is responsible for many important properties of graphene such as high electron mobility and conductivity. SOC opens a gap at the Dirac point, leading to a topological insulating phase, although the gap is too small to support accessible quantum spin Hall effect experimentally [16]. Like graphene, its elemental analogues—silicene, germanene, and stanene, which are proposed by first-principles—also have

Dirac points located at the K and K' in the Brillouin zone in the absence of SOC. However, they are expected to be topological insulators considering SOC, because they have larger SOC due to their buckled honeycomb structure and higher atomic numbers [27–29]. Besides honeycomb lattice, recent studies show that Dirac materials can have very different crystalline lattices and be composed of different elements. Moreover, a Dirac cone can be located not only at high symmetry points like the K and K' points at the corners in the Brillouin zone but also along high symmetry lines or even at generic points in the Brillouin zone [30]. For example, graphynes represent a class of 2D carbon allotropes, which differ from graphene by the presence of triple bonds into their lattice structure. First-principles calculations and tight-binding methods show that α graphyne features Dirac cones at the high-symmetry K and K' points, whereas β graphyne has its Dirac cones located along the high-symmetry Γ -M line [31]. Dirac cones in rectangular $pmmn$ -boron, B_2S honeycomb monolayer, and TiB_2 monolayer are also located along high-symmetry lines, while the organic conductor α -(BEDT-TTF) $_2I_3$ has Dirac cones located at generic points in the Brillouin zone [32–34].

However, compared to hundreds of 2D materials which have been found experimentally or computationally up to now, only a few systems have been predicted to be 2D Dirac materials [35,36]. The search for new 2D Dirac materials is still a current hotspot.

Very recently, researchers identified a novel stable CO nanosheet named $Pm\bar{m}a$ -CO which is a wide direct band-gap semiconductor. Motivated by this, we checked whether there exist other 2D materials formed by isoelectronic counterparts of $Pm\bar{m}a$ -CO [37]. In this paper, we propose an NP monolayer with $Pm\bar{m}a$ structure, which is a Dirac semimetal due to band inversion compared to CO monolayer with the same structure. The Dirac nodes in NP monolayer are located along high symmetry lines and are protected by mirror-reflection symmetry in the absence of SOC. Taking into account SOC,

^{*}Corresponding author: yznjie@csu.edu.cn[†]Corresponding author: guogh@mail.csu.edu.cn

NP monolayer is a topological insulator, although the gap is very small due to the rather weak SOC.

II. COMPUTATIONAL METHODS

Our first-principles calculations are carried out in the framework of density-functional theory (DFT) [38] within the Perdew-Burke-Ernzerhof generalized gradient approximation (PBE) [39]. We perform electronic structures calculations using software package OpenMX [40,41], which is based on norm-conserving pseudopotential and pseudoatomic orbital basis functions. The pseudopotentials are N-PBE13 and P-PBE13, respectively. The pseudoatomic orbital basis sets (N6.0-s2p2d1 and P8.0-s2p2d10), $16 \times 16 \times 1$ k -point mesh, and energy cutoff (200 Ry) have been carefully checked. In our calculations, the primitive cell with $c = 20$ Å along the z direction is fixed. Both the lattice parameters and the positions of all atoms are relaxed until the force is less than 0.01 eV/Å. The phonon frequencies are computed using density-functional perturbation theory (DFPT) [42], which is implemented in QUANTUM ESPRESSO code [43]. We also perform canonical molecular dynamics (MD) simulations at different temperatures from 300 K to 1000 K with a supercell of 100 atoms. The length of time-step of 2 fs and simulations with 1500 steps are executed. To confirm our prediction, band structures calculations are also performed using the hybrid HSE06 functional.

III. RESULTS AND DISCUSSION

Recent studies show that CO monolayer containing two C and two O atoms in a rectangular primitive cell can form a stable structure with nonsymmorphic space group $Pmma$ (No. 51), and the optimized lattice constants are $a = 2.64$ Å and $b = 2.27$ Å [37]. We build and study NP monolayer with the same structure, as shown in Fig. 1(a). The unit cell of NP (CO) monolayer contains N (O) and P (C) atoms located at $2f$ and $2e$ Wyckoff positions, respectively. First, we perform geometric optimization and the calculated lattice constants are $a = 3.611$ Å and $b = 2.733$ Å. Note that there exist reports about monolayer NP with honeycomb, $Pmn21$, and $P21/c$ structures [44–46]. We calculate cohesive energies to compare their stability. The calculated cohesive energy of $Pmma$ -NP, 4.29 eV/atom, is lower than 4.41 eV/atom ($Pmn21$) but higher than 4.13 eV/atom ($P21/c$) and 4.08 eV/atom (honeycomb structure). It suggests that $Pmma$ -NP is less stable than $Pmn21$ -NP but more stable than others. Next, the mechanical and thermal stability of $Pmma$ -NP are confirmed by phonon dispersion and molecular dynamics simulations. The calculated phonon dispersions indicate that $Pmma$ -NP monolayer is mechanical stable because no imaginary frequency appears [Fig. 1(b)]. Snapshots of the final configurations for MD simulations suggest that the system holds the thermal stability at 800 K [Fig. 1(b)]. While at 1000 K, some bonds are broken and the system experiences disruption.

Then we calculate the electronic structure of the NP monolayer. The band structure exhibits the Dirac point along the high symmetry line Γ -Y, as depicted in Fig. 2(a). The existence of the Dirac point is confirmed by the hybrid HSE06

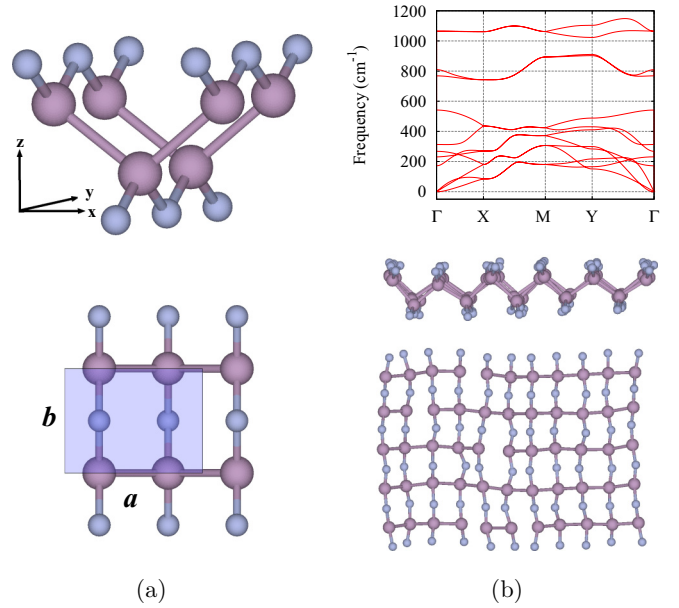


FIG. 1. (a) Side and top views of the optimized structure of orthorhombic $Pmma$ -NP with two N atoms and two P atoms in per primitive cell. The lattice constants of $Pmma$ -NP are $a = 3.611$ Å, $b = 2.733$ Å, and $c = 20$ Å, respectively. N atoms are at $2f$ sites, i.e., $(1/4, 1/2, z_1)$ and $(3/4, 1/2, -z_1)$, while P atoms are at $2e$ sites, $(1/4, 0, z_2)$ and $(3/4, 0, -z_2)$, with $z_1 = 0.078$ and $z_2 = 0.035$. (b) Top: Phonon dispersion of $Pmma$ -NP. Middle and bottom: Snapshots of the final configurations for molecular dynamics simulations at 800 K (side and top views).

functional calculated band structure, as we will discuss later. The projected band structures show that the valence band and conduction band are mainly constituted by $p_z^1 + p_z^2$ of P atoms and $p_x^1 - p_x^2$ of N atoms, respectively, as shown in Figs. 2(b) and 2(c). The superscripts 1 and 2 mean two orbitals from the same kind of two atoms. The linear combinations $+/-$ are derived from first-principles calculations. For comparison, we also calculate the electronic structure of the CO monolayer with the same structure. Our results show that CO monolayer is a semiconductor, which is consistent with the previous study [37], as shown in Fig. 2(d). The projected band structures suggest that the valence band and conduction band are mainly constituted by $p_x^1 - p_x^2$ of O atoms and $p_z^1 + p_z^2$ of C atoms, respectively [see Figs. 2(e) and 2(f)]. The group of wave vectors at the Γ point is D_{2h} . The valence band and conduction band of NP monolayer are irreducible representation of D_{2h} point group labeled by B_{1u} and B_{2g} , respectively, while for CO monolayer, its valence band and conduction band are B_{2g} and B_{1u} , respectively. Figure 3 shows energy levels at the Γ point for CO monolayer and NP monolayer. The band inversion is due to the number of electrons in outer shells of these atoms and the electronegativity difference between them. For CO monolayer, there are six electrons in outer shells of O atom and four electrons in outer shells of C atom. The electronegativity of O is larger than C. It results in occupation of p_x orbitals of O atom and the p_z orbitals of C atom is not occupied. For NP monolayer, both atoms have five electrons in their outer shells, and the electronegativity difference between N atom and P atom is smaller than that between O atom and

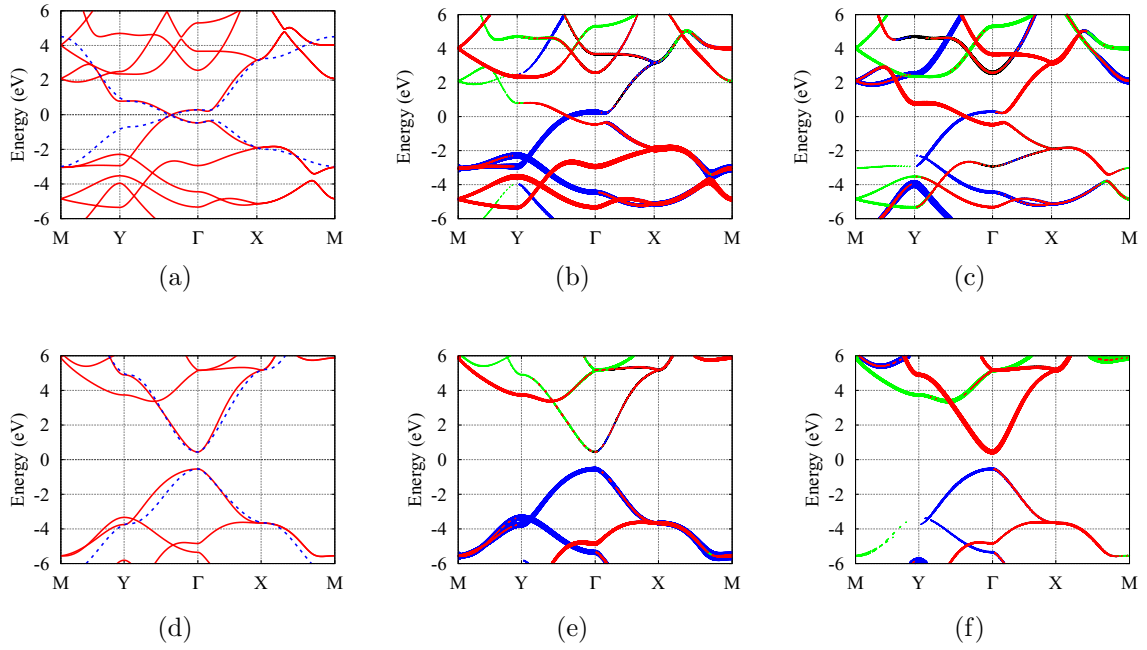


FIG. 2. (a) Band structure of NP monolayer. (b) and (c) show band structure of monolayer NP projected to N and P atomic orbitals, respectively. (d) Band structure of CO monolayer. (e) and (f) show band structures projected to O and C atomic orbitals, respectively. (a) and (d) also show the band structures calculated from the two-band tight-binding model with dashed lines in blue color. The s , p_x , p_y , and p_z orbitals are denoted by black, blue, green, and red colors, respectively. The thickness of the bands is proportional to the orbital weight. The Brillouin zone is rectangular. Γ (0, 0), X (0.5, 0), Y (0, 0.5), and M (0.5, 0.5) are the high symmetric points.

C atom. Therefore, electrons occupy partly p_x orbitals of N atom and partly p_z orbitals of P atom. These result in the band inversion at the Γ point (Fig. 3). Along Γ -Y line, the two bands are still constituted by $p_z^1 + p_z^2$ of P atoms and $p_x^1 - p_x^2$ of N atoms, respectively. They cross each other and form a Dirac cone due to the band inversion. There is another Dirac cone located along Γ -Y line due to time-reversal symmetry. On the contrary, along Γ -X line the two bands belong to the same irreducible representation. Therefore they repel each other and no crossing occurs. The D_{2h} point group is an Abelian group. All irreducible representations are one dimensional for symmorphic space groups where the symmetry operations of the group of the wave vectors are simply point group operations. However, the effect of the glide planes in nonsymmorphic space groups on the group of the wave vector may cause energy bands to stick together along some

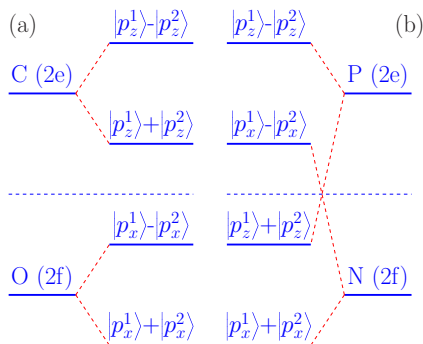


FIG. 3. (a) Energy level of CO monolayer. (b) Energy level of NP monolayer. The blue dashed lines represent the Fermi energy.

of the high symmetry lines in the Brillouin zone. In the case of NP(CO) monolayer, band sticking along X-M is due to glide mirror symmetry of the nonsymmorphic space group [47].

It is well known that band structure calculations at PBE level might overestimate the band inversion due to the underestimation of the band gap. To confirm our prediction, we also perform band structure calculations using the hybrid HSE06 functional. The results show that NP monolayer is still a Dirac semimetal when the hybrid HSE06 functional is used [see Fig. 4(a)]. Now we explore the strain effect on the electronic structures of NP monolayer. The band structures of NP monolayer under different strains are also calculated at HSE06 level (see Fig. 4). As is known, strain can be used to engineer electronic states. For example, the band structure under -12% strain along the y direction indicates that the Dirac point is not at the Fermi level due to the conduction band at the Γ point lower to the Fermi level [see Fig. 4(f)], while under 6% strain along the y direction, there is almost another band crossing at the Γ -X line [see Fig. 4(h)], and the two bands along Γ -X line separate again under stronger strain [see Fig. 4(i)]. However, the calculated electronic structures show the stability of Dirac cone located along Γ -Y line, although the Dirac point may move along Γ -Y line according to the strain.

We also calculate the in-plane stiffness by studying the total energy under strains along two separate directions to check the mechanical anisotropy. The calculated two-dimensional elastic moduli C_{2d} are 67.9N/m and 286.6N/m along the x and y directions, respectively. For comparison, we also calculated C_{2d} of $Pmma$ -CO monolayer. They are 229.7N/m and 477.2N/m , which are in good agreement with previously reported 215.1N/m and 475.7N/m [37]. The results show that

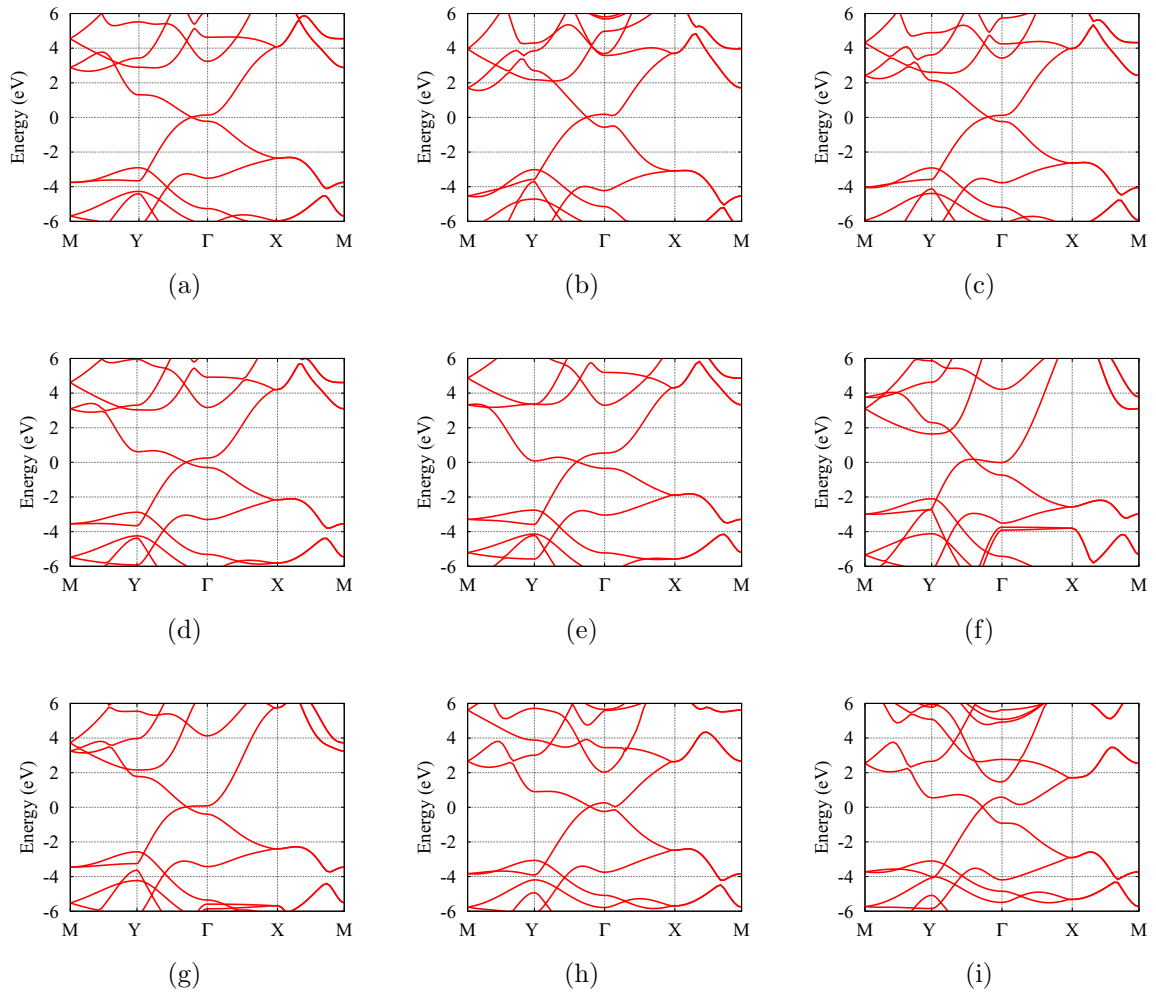


FIG. 4. Band structures calculated using the hybrid HSE06 functional. (a) Intrinsic NP monolayer, and NP monolayer under different strains: (b) -12% , (c) -6% , (d) 6% , (e) 12% , along the x direction; (f) -12% , (g) -6% , (h) 6% , (i) 12% , along the y direction.

Pmma-NP monolayer has a larger anisotropy than *Pmma*-CO monolayer, and a similar anisotropy to phosphorene, which C_{2d} are $24.26N/m$ and $103.28N/m$ [48]. NP (CO) has an anisotropic orthorhombic structure that is ductile along one of the in-plane crystal directions but stiff along the other, because the monolayer can exhibit strain in the x direction by changing the angles between N-N bonds (and P-P bonds) and the x direction because of its structure, while it has to change the length of N-N bond (and P-P bond) to exhibit strain in the y direction. In other words, the stretching of the system along the x direction can be achieved via bond rotation, while the stretching along the y direction requires the changing of bond lengths. The case is similar to phosphorene and other systems with similar structures [49,50].

We calculate electronic structures under different electric fields perpendicular to the monolayer. The results indicate that Dirac point is also stable under electric fields. Figure 5(a) shows the band structure under electric field of 1 V/\AA . The effect of strain and electric fields on the band energy can be understood according to tight-binding model and symmetry analysis as we will discuss later.

The SOC is expected to open a gap at the Dirac point, but the SOC of NP is so small (3.4 meV) that the gap can

be neglected. We calculate electronic structures with modified SOC strength. Figure 5(b) shows the band structure with SOC 50 times greater than the intrinsic SOC of NP monolayer. A gap is opened due to SOC. Because of the presence of both time-reversal symmetry and inversion symmetry, the \mathbb{Z}_2 invariant can be determined from the knowledge of the parity of the occupied states at the time-reversal invariant momenta in the Brillouin zone [16]. There are four time-reversal invariant momenta for orthorhombic structure, i.e., Γ ,

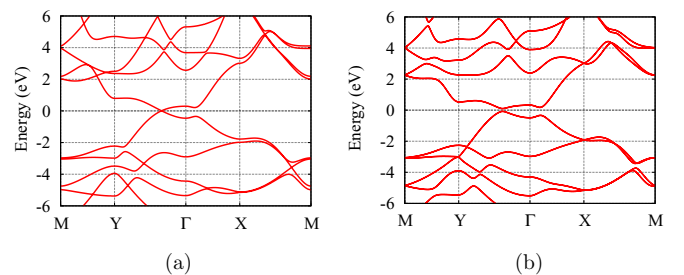


FIG. 5. (a) Band structure of NP monolayer under electric field 1 V/\AA . (b) Band structure of monolayer NP with SOC 50 times greater than its intrinsic SOC.

TABLE I. The parity at each time-reversal invariant k point and \mathbb{Z}_2 indices of CO and NP monolayers.

CO monolayer					NP monolayer				
Γ	+	-	+	+	Γ	+	-	+	+
X	+	-	+	-	X	+	-	+	-
Y	+	-	+	+	Y	+	-	+	+
M	+	-	+	-	M	+	-	+	-
\mathbb{Z}_2 invariant $\nu = 0$					\mathbb{Z}_2 invariant $\nu = 1$				

X, Y, and M points. The band inversion at Γ means topological invariants \mathbb{Z}_2 changing, because the parity of valence band and conduction band, i.e., B_{2g} and B_{1u} , are opposite. Direct parity counting at time reversal invariant momenta shows that the \mathbb{Z}_2 is 0 for CO monolayer and 1 for monolayer NP (see Table I). Therefore, CO monolayer is a band insulator and NP monolayer is a topological insulator.

To gain a deeper understanding of the electronic structures of NP and CO monolayers and the stability of Dirac point in NP band dispersion, we construct a tight-binding model to describe the two monolayers. As there are only two bands between ± 2 eV around Fermi energy, this enables us to construct a minimal two-band model. From first-principles calculations, the valence and conduction bands are mainly constituted by $p_x^1 - p_x^2$ from $2f$ sites and $p_z^1 + p_z^2$ from $2e$ sites. They belong to B_{2g} and B_{1u} irreducible representation of D_{2h} . We use these irreducible representations to construct low-energy Hamiltonian

$$|\psi_u\rangle = |p_z^1\rangle + |p_z^2\rangle, |\psi_g\rangle = |p_x^1\rangle - |p_x^2\rangle. \quad (1)$$

The minimal Hamiltonian for such a system is given by [30]

$$\hat{H}(\mathbf{k}) = d_0(\mathbf{k})\sigma_0 + \mathbf{d}(\mathbf{k}) \cdot \hat{\sigma} \quad (2)$$

with the matrix elements

$$\begin{aligned} d_0(\mathbf{k}) &= \frac{\epsilon_1 + \epsilon_2}{2} + (V_{s,x} + V_{p,x})\cos(k_x) + (V_{s,y} + V_{p,y})\cos(k_y) \\ d_x(\mathbf{k}) &= 0 \\ d_y(\mathbf{k}) &= 2V_{sp}\sin(k_x) \\ d_z(\mathbf{k}) &= \frac{\epsilon_1 - \epsilon_2}{2} + (V_{s,x} - V_{p,x})\cos(k_x) + (V_{s,y} - V_{p,y})\cos(k_y), \end{aligned} \quad (3)$$

TABLE II. The tight-binding parameters fitting to first-principles calculations (in eV).

	ϵ_1	ϵ_2	$V_{s,x}$	$V_{s,y}$	$V_{p,x}$	$V_{p,y}$	V_{sp}
NP	2.02	-1.35	-0.93	-0.31	0.57	0.25	0.25
CO	5.05	-3.68	-1.19	-1.11	0.78	0.79	0.70

where ϵ_1 and ϵ_2 are onsite energies of $|\psi_u\rangle$ and $|\psi_g\rangle$ orbitals, and $V_{s,x}$ and $V_{s,y}$ are nearest-neighbor hopping in the x and y directions of $|\psi_u\rangle$ orbitals, respectively. $V_{p,x}$ and $V_{p,y}$ are nearest-neighbor hopping in the x and y directions of $|\psi_g\rangle$ orbitals, respectively, and V_{sp} is the nearest-neighbor hopping parameter that hybridizes the $|\psi_u\rangle$ and $|\psi_g\rangle$ orbitals. σ_0 is identity matrix and $\hat{\sigma}$ is Pauli matrix. The two energy bands of the Hamiltonian of Eq. (2) can be described by

$$E_{\pm}(\mathbf{k}) = d_0(\mathbf{k}) \pm |\mathbf{d}(\mathbf{k})|. \quad (4)$$

Adjusting the onsite energy, the system can exhibit phase transformation between Dirac semimetal and band insulator, corresponding to NP monolayer and CO monolayer, respectively.

The condition for Dirac point is $|\mathbf{d}(\mathbf{k})| = 0$, i.e., $d_z(\mathbf{k}) = 0$ and $d_y(\mathbf{k}) = 0$. That means $|\frac{\epsilon_1 - \epsilon_2}{2} + (V_{s,x} - V_{p,x})| < |V_{s,y} - V_{p,y}|$ or $|\frac{\epsilon_1 - \epsilon_2}{2} - (V_{s,x} - V_{p,x})| < |V_{s,y} - V_{p,y}|$, and $k_x = 0$. The parameters in this tight-binding model are fitted to first-principles calculations (see Table II). The Dirac point condition holds for NP monolayer. While for CO monolayer, the condition does not hold. We also plot the band structure in comparison with the first-principles bands in Figs. 2(a) and 2(d). One can see that the tight-binding model captures the essential features of the low-energy electronic structure.

The Hamiltonian of the two-band model is mirror symmetric under x reflection. The corresponding mirror-reflection operator is $R = \sigma_z$, so that $R\hat{H}(k_x, k_y)R^{-1} = \hat{H}(-k_x, k_y)$. The only mass term that can open a gap is σ_x . However, this mass term is forbidden by mirror-reflection symmetry, because $R\sigma_x R^{-1} = -\sigma_x$. Therefore, the Dirac cones are stable and protected by the mirror-reflection symmetry along the x direction. However, they are not globally stable: Two Dirac cones can annihilate at time invariant momenta point and open a gap. It is obvious that strain engineering along the x or y direction does not break the mirror-reflection symmetry. Therefore, strain engineering cannot destroy Dirac points but

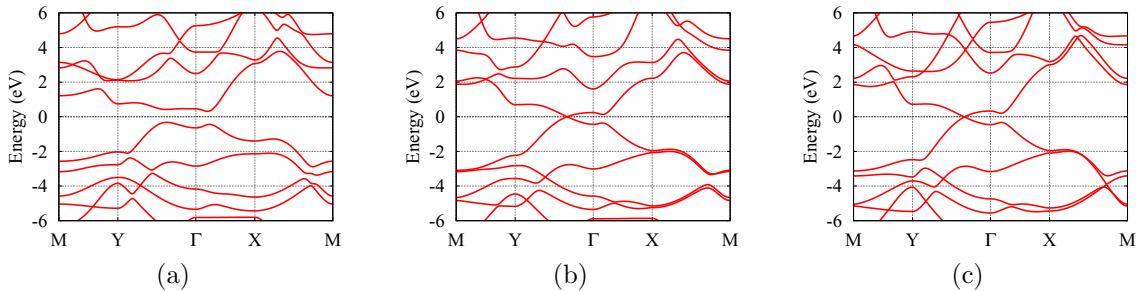


FIG. 6. (a) Band structure of NP monolayer with one N atom displaced along the x direction from (0.25, 0.5, 0.578) to (0.35, 0.5, 0.578). (b) Band structure of monolayer NP with one N atom displaced along the y direction from (0.25, 0.5, 0.578) to (0.25, 0.6, 0.578). (c) Band structure of NP monolayer with one N atom displaced along the z direction from (0.25, 0.5, 0.578) to (0.25, 0.5, 0.573).

only move Dirac points due to the changing of parameters. Note that the bands degeneracy along $X-M$ remains due to the glide symmetry, as shown in Fig. 4. The electric field does not open a gap for the same reason. In general, the electric field perpendicular to the material modifies the onsite energies in the tight-binding Hamiltonian. The electric field along the z direction does not break mirror-reflection symmetry along the x direction. However, the band degeneracy along the $X-M$ is lifted due to the breaking of glide symmetry, as shown in Fig. 5(a). By comparison, the Dirac cones in silicene at the K and K' points are protected by sublattice symmetry. The electric field perpendicular to the monolayer breaks the sublattice symmetry, therefore opens a gap in silicene [51].

To confirm the Dirac condition, we move the position of one N atom in the primitive cell along x , y , and z directions, respectively. When the N atom is displaced along the x direction, therefore the mirror-reflection symmetry is broken; the gap is opened in dispersion. While the N atom is displaced along the y or z direction, which does not break the mirror-reflection symmetry, the Dirac cone remains. However, the bands sticking along $X-M$ is lifted because of the breaking of glide symmetry, as shown in Fig. 6.

IV. CONCLUSIONS

In conclusion, we predict, based on first-principles calculations, that the NP monolayer with an orthorhombic $Pmma$ structure is a Dirac semimetal. Phonon dispersions and molecular dynamics simulations suggest that it is stable up to 800 K. The band structure of $Pmma$ -NP exhibits a pair of anisotropic Dirac points along high symmetry lines Γ -Y and Γ - Y . The calculated in-plane stiffness suggests large mechanical anisotropy similar to phosphorene. Our calculations indicate that the Dirac cone is stable under strains or electric fields. To gain insight into the stability of Dirac point, we construct a two-band model to describe the valence band and conduction band and demonstrate that the Dirac cones are locally stable due to the mirror-reflection symmetry along the x direction. We hope that our work will promote the research aiming at the synthesis of the new 2D Dirac material and the search for new 2D topological materials.

ACKNOWLEDGMENTS

We wish to acknowledge the support of the National Natural Science Foundation of China No. 11674400 and No. 11704415.

-
- [1] K. S. Novoselov, A. K. Geim, S. V. Morozov, D. Jiang, Y. Zhang, S. V. Dubonos, I. V. Grigorieva, and A. A. Firsov, *Science* **306**, 666 (2004).
- [2] E. V. Castro, N. M. R. Peres, T. Stauber, and N. A. P. Silva, *Phys. Rev. Lett.* **100**, 186803 (2008).
- [3] A. H. Castro Neto, F. Guinea, N. M. R. Peres, K. S. Novoselov, and A. K. Geim, *Rev. Mod. Phys.* **81**, 109 (2009).
- [4] X. Wu, J. Dai, Y. Zhao, Z. Zhuo, J. Yang, and X. C. Zeng, *ACS Nano* **6**, 7443 (2012).
- [5] A. Kormányos, V. Zólyomi, N. D. Drummond, P. Rakyta, G. Burkard, and V. I. Fal'ko, *Phys. Rev. B* **88**, 045416 (2013).
- [6] H. Liu, A. T. Neal, Z. Zhu, Z. Luo, X. Xu, D. Tománek, and P. D. Ye, *ACS Nano* **8**, 4033 (2014).
- [7] V. O. Özçelik, O. U. Aktürk, E. Durgun, and S. Ciraci, *Phys. Rev. B* **92**, 125420 (2015).
- [8] L.-M. Yang, V. Bačić, I. A. Popov, A. I. Boldyrev, T. Heine, T. Frauenheim, and E. Ganz, *J. Am. Chem. Soc.* **137**, 2757 (2015).
- [9] L. Kou, Y. Ma, C. Tang, Z. Sun, A. Du, and C. Chen, *Nano Lett.* **16**, 7910 (2016).
- [10] S. M. Young and C. L. Kane, *Phys. Rev. Lett.* **115**, 126803 (2015).
- [11] B. Wang, S. Yuan, Y. Li, L. Shi, and J. Wang, *Nanoscale* **9**, 5577 (2017).
- [12] J. Yang, S. Song, S. Du, H.-J. Gao, and B. I. Yakobson, *J. Phys. Chem. Lett.* **8**, 4594 (2017).
- [13] H. Zhang, Y. Xie, Z. Zhang, C. Zhong, Y. Li, Z. Chen, and Y.-P. Chen, *J. Phys. Chem. Lett.* **8**, 1707 (2017).
- [14] B. Yang, X. Zhang, and M. Zhao, *Nanoscale* **9**, 8740 (2017).
- [15] C. Wang, Q. Xia, Y. Nie, and G. Guo, *J. Appl. Phys.* **117**, 124302 (2015).
- [16] L. Fu and C. L. Kane, *Phys. Rev. B* **76**, 045302 (2007).
- [17] S. M. Young, S. Zaheer, J. C. Y. Teo, C. L. Kane, E. J. Mele, and A. M. Rappe, *Phys. Rev. Lett.* **108**, 140405 (2012).
- [18] J. Hu, Z. Tang, J. Liu, X. Liu, Y. Zhu, D. Graf, K. Myhro, S. Tran, C. N. Lau, J. Wei, and Z. Mao, *Phys. Rev. Lett.* **117**, 016602 (2016).
- [19] M. G. Vergniory, L. Elcoro, F. Orlandi, B. Balke, Y.-H. Chan, J. Nuss, A. P. Schnyder, and L. M. Schoop, *Eur. Phys. J. B* **91**, 213 (2018).
- [20] K.-H. Jin, H. Huang, Z. Wang, and F. Liu, *Nanoscale* **11**, 7256 (2019).
- [21] S. A. Yang, H. Pan, and F. Zhang, *Phys. Rev. Lett.* **113**, 046401 (2014).
- [22] N. P. Armitage, E. J. Mele, and A. Vishwanath, *Rev. Mod. Phys.* **90**, 015001 (2018).
- [23] T. O. Wehling, A. M. Black-Schaffer, and A. V. Balatsky, *Adv. Phys.* **63**, 1 (2014).
- [24] C. L. Kane and E. J. Mele, *Phys. Rev. Lett.* **95**, 226801 (2005).
- [25] B. A. Bernevig, *Topological Insulators and Topological Superconductors* (Princeton University Press, Princeton, 2013).
- [26] O. I. Malyi, K. V. Sopiha, and C. Persson, *ACS App. Mater. Interfaces* **11**, 24876 (2019).
- [27] C.-C. Liu, W. Feng, and Y. Yao, *Phys. Rev. Lett.* **107**, 076802 (2011).
- [28] V. Zólyomi, J. R. Wallbank, and V. I. Fal'ko, *2D Mater.* **1**, 011005 (2014).
- [29] M. Ezawa, *J. Phys. Soc. Jpn.* **84**, 121003 (2015).
- [30] G. van Miert and C. M. Smith, *Phys. Rev. B* **93**, 035401 (2016).
- [31] G. van Miert, V. Juričić, and C. Morais Smith, *Phys. Rev. B* **90**, 195414 (2014).

- [32] X.-F. Zhou and H.-T. Wang, *Adv. Phys.: X* **1**, 412 (2016).
- [33] A. Kobayashi, S. Katayama, Y. Suzumura, and H. Fukuyama, *J. Phys. Soc. Jpn.* **76**, 034711 (2007).
- [34] Y. Zhao, X. Li, J. Liu, C. Zhang, and Q. Wang, *J. Phys. Chem. Lett.* **9**, 1815 (2018).
- [35] S. Lebègue, T. Björkman, M. Klintonberg, R. M. Nieminen, and O. Eriksson, *Phys. Rev. X* **3**, 031002 (2013).
- [36] Y. Ren, Z. Qiao, and Q. Niu, *Rep. Prog. Phys.* **79**, 066501 (2016).
- [37] Z.-W. Teng, C.-S. Liu, and X.-H. Yan, *Nanoscale* **9**, 5445 (2017).
- [38] W. Kohn and L. J. Sham, *Phys. Rev.* **140**, A1133 (1965).
- [39] J. P. Perdew, K. Burke, and M. Ernzerhof, *Phys. Rev. Lett.* **77**, 3865 (1996).
- [40] T. Ozaki and H. Kino, *Phys. Rev. B* **72**, 045121 (2005).
- [41] Y.-T. Lee and T. Ozaki, *J. Mol. Graphics Modell.* **89**, 192 (2019).
- [42] S. Baroni, P. Giannozzi, and A. Testa, *Phys. Rev. Lett.* **58**, 1861 (1987).
- [43] P. Giannozzi, S. Baroni, N. Bonini, M. Calandra, R. Car, C. Cavazzoni, Davide Ceresoli, G. L. Chiarotti, M. Cococcioni, I. Dabo, A. D. Corso, S. d. Gironcoli, S. Fabris, G. Fratesi, R. Gebauer, U. Gerstmann, C. Gougoussis, Anton Kokalj, M. Lazzeri, L. Martin-Samos, N. Marzari, F. Mauri, R. Mazzarello, Stefano Paolini, A. Pasquarello, L. Paulatto, C. Sbraccia, S. Scandolo, G. Sclauzero, A. P. Seitsonen, A. Smogunov, P. Umari, and R. M. Wentzcovitch, *J. Phys.: Condens. Matter* **21**, 395502 (2009).
- [44] L. Zhao, W. Yi, J. Botana, F. Gu, and M. Miao, *J. Phys. Chem. C* **121**, 28520 (2017).
- [45] H. Xiao, F. Hao, X. Liao, X. Shi, Y. Zhang, and X. Chen, *arXiv:1603.01957*.
- [46] Y. Nie, M. Rahman, P. Liu, A. Sidike, Q. Xia, and G.-h. Guo, *Phys. Rev. B* **96**, 075401 (2017).
- [47] M. S. Dresselhaus, G. Dresselhaus, and A. Jorio, *Group Theory: Application to the Physics of Condensed Matter* (Springer-Verlag, Berlin, 2008).
- [48] J. Xiao, M. Long, X. Zhang, J. Ouyang, H. Xu, and Y. Gao, *Sci. Rep.* **5**, 9961 (2015).
- [49] V. Sorkin and Y. W. Zhang, *2D Mater.* **2**, 035007 (2015).
- [50] P. Liu, Y.-z. Nie, Q.-l. Xia, and G.-h. Guo, *Phys. Lett. A* **381**, 1102 (2017).
- [51] N. D. Drummond, V. Zólyomi, and V. I. Fal'ko, *Phys. Rev. B* **85**, 075423 (2012).